Applied Microscopy
Korean Society of Microscopy
pISSN 2287-5123 · eISSN 2287-4445
http://dx.doi.org/10.9729/AM.2012.42.3.164

Direct Determination of Cationic Disordering in Sodium Bismuth Titanate

Si-Young Choi*, Yuichi Ikuhara[1]

Korea Institute of Materials Science (KIMS), Changwon 642-831, Korea
[1]Institute of Engineering Innovation, The University of Tokyo, Tokyo 113-8656, Japan

*Correspondence to:
Choi SY,
Tel: +82-55-280-3514
Fax: +82-55-280-3699
E-mail: youngchoi@kims.re.kr

Received August 11, 2012
Revised September 6, 2012
Accepted September 10, 2012

The relaxor ferroelectric feature in lead-free perovskite oxides, where the dipoles are randomly oriented and they can be feasibly aligned parallel to the external bias, is attracting lots of attention in the field of piezoelectric materials science, since it is one of candidates to replace the toxic lead-based materials that are still being commercially used. However, the origin of relaxor characteristic and its related atomic structure are still ambiguous. In this study, $Na_{1/2}Bi_{1/2}TiO_3$, chosen as a model relaxor system, was found to exhibit a cationic-disordered atomic structure; and furthermore the nonpolar atomic structure and its related oxygen tilting were ascertained via annular bright field imaging skill. We also found that this cationic disordering gives rise to the local formation of atomic vacancies.

Key Words: Sodium bismuth titanate, Point defect, Relaxor, Ferroelectric, Aberration-corrected STEM

INTRODUCTION

Sodium bismuth titanate, $Na_{1/2}Bi_{1/2}TiO_3$ (NBT), is known to be a typical relaxor perovskite and has been extensively investigated for its potential applications to actuators, sensors, and transducers (Siny et al., 1991; Tu et al., 1994; Jones & Thomas, 2000; Kreisel et al., 2000; Xu & Ching, 2000; Kreisel et al., 2001; Petzelt et al., 2004; Dorcet & Troillard, 2008). NBT exhibits the peculiar ferroelectric property as a function of temperature: the ferroelectric below 200°C, antiferroelectric up to 320°C, and paraelectirc above 320°C. On the contrary to the phase transition, in terms of crystallography, four kinds of phases related with three phase transition arise during the temperature sequence: rhomoboheral below 200°C, tetragonal & rhombohedral up to 320°C, tetragonal up to 520°C, and cubic above 520°C. More interestingly, the broad frequency dependent permittivity vs. temperature in NBT strongly arise the possibility of its relaxor ferroelectricity even though the large coercive electric field and remnant polarization in NBT imply the strong ferroelectricity at room temperature. The relaxor behavior in complex perovskite oxides has been mostly studied in lead-based perovskites such as $Pb(Mg_{1/3}Nb_{2/3})O_3$, $Pb(Sc_{1/2}Ta_{1/2})O_3$ and $Pb_{1-x}La_x(Zr_yTi_{1-y})O_3$ (Smolenskii et al., 1961a; Chu et al., 1993; Dai et al., 1994; Krunmins et al., 1994); relaxor property is explained to be attributed to nano polar cluster with a cationic ordering, which is embedded in the nonpolar matrix with a cationic disordering. In addition, homovalent solid solutions, such as $Ba(Ti_{1-x}Zr_x)O_3$ and $Ba(Ti_{1-x}Sn_x)O_3$, also exhibit a relaxor characteristic with compositional disorder (Sciau et al., 2000; Simon et al., 2004; Yasuda et al., 1996). However, in case of NBT, the origin of relaxor ferroelectricity is still controversial; the relaxor ferroelectricity is said to be induced by the polar nanoregions (PNRs) just like in the lead-based perovskites (Tai & Lereah, 2009; Yao et al., 2012), while third-party phase, such as a modulated orthorhombic phase mediating between rhombohedral and tetragonal, is reported to plays a crucial role in the relaxor property (Dorcet et al., 2008a, 2008b; Levin & Reaney, 2012).

To unveil the mysterious ferroelectricity in NBT, it is

indispensable to firstly verify the existence of a superlattice, where chemical ordering of A-site species (Na and Bi) occurs, since the cationic ordering at room temperature more likely gives rise to the ferroelectricity rather than relaxor property. With regard to the ordered NBT structure, the criss-cross superlattice (Fig. 1A) has been found to be energetically stable by using first principle calculations (Burton & Cockayne, 2001); however, in general, the NaCl-type ordering of Na and Bi cations (Fig. 1B) seems more reasonable because it is the stable crystal structure for equal numbers of positively charged ions and negatively charged ions on a simple cubic structure. Once the superlattice is formed by compositional ordering of Na and Bi, the criss-cross or NaCl-type ordering structure is assumed to create a noticeable superlattice peak in the diffraction pattern. From this viewpoint, the compositional ordering/disordering of NBT has also been studied using statistical analysis tools such as X-ray diffraction (XRD), neutron diffraction, and Raman spectra (Vakhrushev et al., 1985; Siny et al., 1991; Park et al., 1994; Chiang et al., 1998; Jones & Thomas, 2002). Park et al. (1994) have observed weak superlattice single crystal XRD reflections and attributed them to the compositional ordering of Na and Bi cations. In contrast, Vakhrushev et al. (1985) observed three structural octahedral tilting behaviors that might be induced by compositional disordering. In addition, a neutron diffraction study on NBT has revealed that it possesses no long range Na-Bi cationic ordering (Jones & Thomas, 2002). Although the compositional ordering of complicated-structured perovskites is feasibly affected by sintering conditions (Bokov et al., 1999) and thus it could be why the cationic ordering/disordering of NBT is still controversial, it is imperative to identify the crystal structure of the prepared NBT under the respective sintering conditions before addressing the piezoelectric properties.

Recent progress in the correction of aberrations in electron microscopy facilitates the visualization of atomic structures even on the sub-angstrom level, and furthermore the intensified electron beam enables the observation of sensitive variations in atomic column images as well as chemical information by energy dispersive spectroscopy and electron energy loss spectroscopy (EELS) (Haider et al., 1998; Batson et al., 2002; Nellist et al., 2004; Lupini & Pennycook, 2007; Chung et al., 2008; Jia et al., 2008; Choi et al., 2009; Chung et al., 2009; Hovden et al., 2010). Therefore, in this study, moving beyond statistical methods, we attempt to visualize the atomic structure of NBT via aberration-corrected scanning transmission electron microscopy (STEM) to determine its availability of cationic ordering and to identify the origin of relaxor ferroelectricity in NBT.

MATERIALS AND METHODS

NBT Sample Preparation

The NBT sample was prepared from commercial powders of Na_2CO_3 (Acros Organics, Fair Lawn, NJ, USA), Bi_2O_3 (Kojundo Chemical Lab Co., Saitama, Japan), and TiO_2 (Sigma-Aldrich, St. Louis, MO, USA). The batched powders were ball-milled for 24 h in ethanol using a polypropylene bottle and 5 mm-sized ZrO_2 balls. After drying the slurry after the milling process, the mixture powder was fired at ~800°C to synthesize the starting NBT powder. Powder compacts of 14 mm diameter and ~4 mm thickness were cold-isostatically pressed at 200 MPa and then sintered at 1,120°C for 4 h on a platinum plate in an alumina crucible in air. The heating and cooling rates were fixed to 4°C/min.

STEM Observation and Image Simulation

The thin foils were prepared using a conventional route including mechanical thinning to ~20 μm and ion beam milling to electron transparency at an acceleration voltage of 2~4 kV using an Ar ion beam. Z-contrast high-angle annular dark-field (HAADF) images were recorded with a scanning transmission electron microscope (JEM-2100F, JEOL, Tokyo, Japan) at 200 kV with a spherical aberration corrector (CEOS GmbH, Heidelberg, Germany), where an electron probe

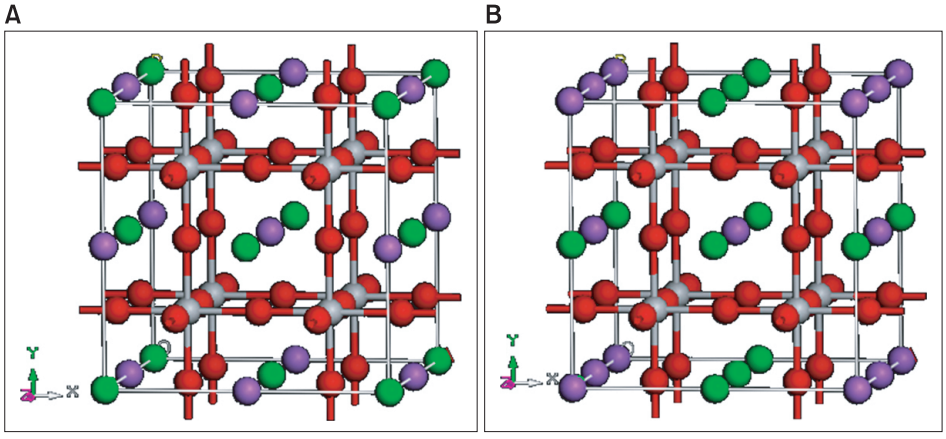

Fig. 1. (A) NaCl-type and (B) criss-cross superlattice structures of $Na_{1/2}Bi_{1/2}TiO_3$, where the green, purple, gray, and red spheres represent sodium, bismuth, titanium, and oxygen atoms, respectively.

size of ~1.0 Å is available. In the HAADF imaging, a probe convergence angle of about 22 mrad and a HAADF detector with an inner angle greater than ~80 mrad were used for clear atomic number (Z)-sensitive images. The contrast of the HAADF-STEM image clearly reflects the A-site compositional information: the intensity in the HAADF-STEM image depends on the atomic number and therefore the Bi (Z_{Bi}=83) atomic column results in brighter contrast than Na (Z_{Na}=11). The obtained raw images were filtered to eliminate background noise using 2-dimensional difference filters (HREM Filters Pro; HREM Research Inc., Higashimastuyama, Japan). HAADF STEM image simulations based on the multislice method were performed using WinHREM (HREM Research Inc.).

EELS Calculation (*O-K* Edge)

To predict the *O-K* edge structure of EELS, calculation was performed by using a commercial program (CASTEP; Accelrys Inc., San Diego, CA, USA). A 2×2×3 supercell was constructed based on the previously reported crystal structure (Jones & Thomas, 2002) and then an electronic hole, namely, a core-hole, was generated at the core-orbital following the one-particle calculation method (Mizoguchi et al., 2010). The electron exchange-correlation potential was described by the generalized gradient approximation in the form of Perdew, Burke and Ernzerhof. Brillouin-zone sampling using a 5×5×6 Monkhorst-Pack mesh was performed for the NBT supercell. It was confirmed that these conditions ensured a good total energy convergence of 2×10^{-6} eV/atom.

RESULTS AND DISCUSSION

In general, a NaCl-type superlattice structure seems to be more reasonable (Siny et al., 1991; Park et al., 1994), since NaCl is the ground state structure for equal numbers of positively charged Na^+ and negatively charged Cl^- on a simple cubic structure; thus Bi^{3+} and Na^{1+} might be able to effectively array like NaCl, giving rise to an average A-site charge of +2. Along with NaCl-typed superlattice, the criss-cross structure, where Na^{1+} and Bi^{3+} cations are arranged perpendicular to [001], was found to be energetically stable by using the first principles calculation on the assumption that NBT has long range cationic ordering (Burton & Cockayne, 2001). Under the assumption that NBT has a superlattice with A-site cationic ordering, a HAADF-STEM image simulation along the [001] projection was performed. Since A-sites are identically occupied by both Na and Bi atoms in a NaCl-type superlattice (inset 'A' in Fig. 2A), the simulated STEM image exhibits only two kinds of atomic contrasts, Na-Bi column and Ti-O column; thus, it resembles a simple perovskite structure such as $BaTiO_3$ and $SrTiO_3$. In the case of the criss-cross superlattice, the simulated STEM image (inset 'B' in Fig. 2A) along the [001] projection shows somewhat complicated contrasts; there are four kinds of atomic contrasts: Bi column, Na column, Na-Bi column, and Ti-O column. Although the crisscross superlattice shows a complicated STEM image, the important feature is that those four atomic contrasts were periodically arrayed and thus the cationic ordering can be easily determined.

Fig. 2A is an HAADF-STEM image of NBT and the inset 'C' is an enlarged image, which appears to exhibit two kinds of contrasts, as described for the NaCl-type superlattice, and therefore this experimental HAADF-STEM image seems to be consistent with the simulated image of the NaCl-type superlattice. This might imply that NBT holds a NaCl-type superlattice, as previously noted in other studies. However,

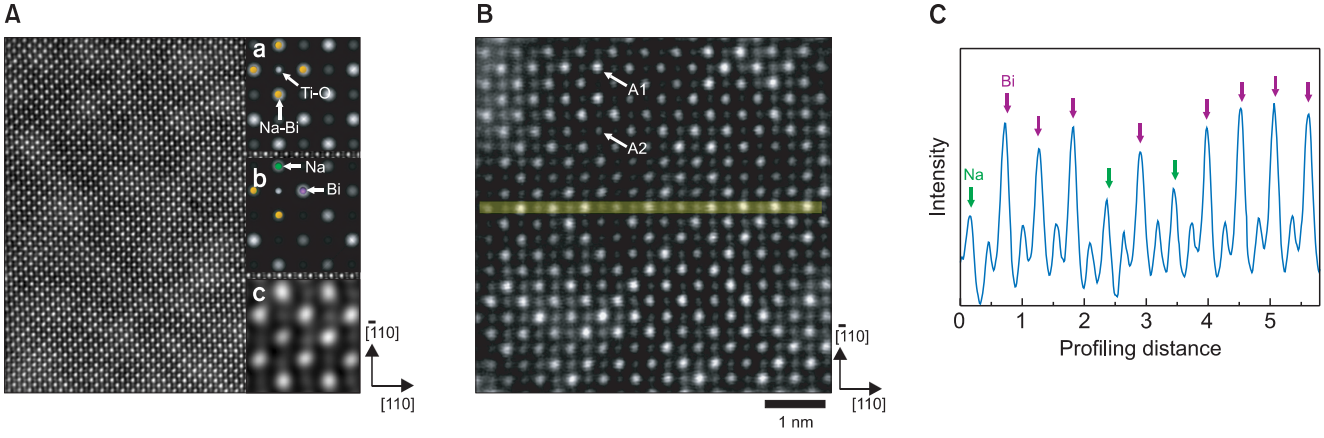

Fig. 2. (A) HAADF-STEM image experimentally obtained from NBT along the [001] projection and the inset image 'c' is a magnified HAADF-STEM image from image. Inset images 'a' and 'c' are simulated HAADF STEM images along the [001] projection from NaCl-type and criss-cross superlattices, respectively. The green, purple, gray, and orange spheres in the insets 'a' and 'b' represent Na, Bi, Ti-O, and Na-Bi atomic columns, respectively. (B) HAADF-STEM image from a thin area showing cationic disordering. (C) Intensity profiles along the [110] direction from the linear region indicated by the yellow rectangle in image (B). HAADF, high-angle annular dark-field; STEM, scanning transmission electron microscopy; NBT, $Na_{1/2}Bi_{1/2}TiO_3$.

the recorded HAADF-STEM image from the thin area (Fig. 2B), the thickness of which was measured to be ~12 nm by using the intensity ratio between the first plasmon-loss and the zero-loss peaks in the electron energy loss spectra, vividly demonstrates that there is no cationic ordering structure. Since the HAADF-STEM image, so-called the Z-contrast image, reflects the chemical information due to its sensitivity to the atomic number (Z), the Bi atom (Z_{Bi}=83) causes much stronger contrast than the Na atom (Z_{Na}=11); therefore, Bi-excess A-site (A1) in Fig. 2B looks much brighter than Na-excess one (A2). Fig. 2C shows the profiled contrast along the [110] direction from the linear area indicated by the yellow rectangle in Fig. 2B. In this profile, all A-sites are indicated by arrows and the weak peaks between the A-site peaks represent the Ti-O atomic columns. A-sites randomly are composed of Na-excess (green arrows) and Bi-excess (purple arrows) sites. The ground state of the complex perovskite, $A'_{1/2}A''_{1/2}BO_3$, must hold a chemically ordered structure because the electrostatic and elastic energies of the superlattice can be minimized in the ordered structure owing to the difference in the charge and the size between A′ and A″ cations. However, thermal activation can destroy the ordering structure and the occurred cationic disordering cannot be changed even by an additional annealing process, as in a $PbMg_{1/3}Nb_{2/3}O_3$ system (Smolenskii et al., 1961b).

Even though it is well known that the rhombohedral phase is stable at room temperature, NBT exhibits both rhombohedral and tetragonal phases. The diversity of NBT phase reflects the difference in the oxygen octahedral tilting, which gives rise to the superlattice reflection in the electron diffraction pattern: 1/2(*ooo*) spots (*o* represents an odd value of the Millers indices) is typical of the rhombohedral supercell with the $a^-a^-a^-$ anti-phase octahedral tilting and 1/2(*ooe*) spots (*e* represents an even value of the Millers indices) indicates the tetragonal supercell with the $a^0a^0c^+$ in-phase octahedral tilting. 1/2(310) spot in the electron diffraction pattern from [001] projection (Fig. 3A) and 1/2(111) spot from [0$\bar{1}$1] projection clearly shows that NBT sample in this study has both rhombohedral and tetragonal phases. Tetragonal phase exhibits a nonpolar structure, where the cationic disordering is expected, while rhombohedral phase is associated with a polar structure having the cationic ordering. 1/2(*ooo*) spots are also related with the cationic ordered tetragonal phase and thus those superlattice spots are observed even at 620°C (Dorcet et al., 2008a, 2008b). Thus, the observed 1/2(*ooo*) spots at high temperature can be explained by the Na/Bi ordered superlattice structure (like a rock salt structure) rather than the survival of rhombohedral phase. On the contrary, we could not trace any 1/2(*oee*) spots in the electron diffraction from [001] projection, which is originated from the orthorhombic phase with the $a^-c^+a^-$ anti-phase octahedral tilting, although this orthorhombic phase was reported to play the role of PNRs together with rhombohedral phase at room temperature (Levin & Reaney, 2012). Therefore, in our study, NBT is the typical relaxor ferroelectric materials of the PNRs of rhombohedral phase surrounded by nonpolar tetragonal phase; and thus the typical behavior of hard P-E curve with a high coercive field and remnant polarization in NBT is thought to be related with nonergodic state (frozen PNRs) (Tagantsev & Galzounov, 1998; Bao et al., 2002).

Although the polar rhombohedral phase with a cationic ordering is expected to exist in NBT, we could not find them due to its small dimensionality. If the size of PNRs is several nanometer scale, it is challenging to observe the locally formed PNRs since the thinnest area in our study was measured to be about 12 nm. Therefore, the local atomic structure in the current work is mainly related with nonpolar tetragonal phase. As the A-site cationic disordering is visualized in Fig. 2B, this cationic disordering is thought to affect the local atomic structure or octahedral tilting. In order to visually examine the actual effect of the compositional disordering, an annular bright field (ABF)-STEM image was simultaneously

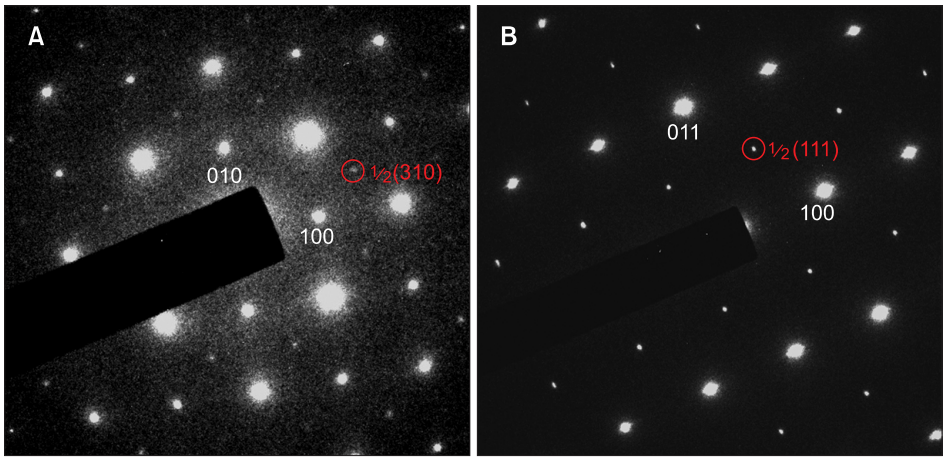

Fig. 3. Selected area electron diffraction patterns recorded along (A) <100> and (B) <110> zone axes. 1/2(*ooe*) and 1/2(*ooo*) reflections appear in <100> and <110> zone axes, respectively.

recorded from the same area together with a HAADF-STEM image, as shown in Fig. 4. Since ABF imaging is capable of visualizing light atoms such as Na and O in NBT (Okunishi et al., 2009; Findlay et al., 2010; Ishikawa et al., 2010; Choi et al., 2012), we can directly observe all component atoms in NBT and determine the exact atomic positions. Fig. 4A and D are the HAADF-STEM images from [001] and [1$\bar{1}$0] projections, respectively. The red rectangle in (a) and the green rectangle in (d) represent the Bi-excess areas, whilst the blue rectangle in (a) and orange one in (d) indicate the Na-excess areas. Enlarged ABF images of the area indicated by the red, blue, green, and orange rectangles are shown in Fig. 4B, C, E, and F, respectively. ABF images along the [001] projection of Fig. 4B and c show no significant atomic displacement, which implies that the recorded Bi-excess and Na-excess atomic structures are associated with the nonpolar tetragonal phases. Careful observation of Fig. 4B and C reveals that the oxygen atoms align along [110] in a zig-zag shape, and thus oxygen octahedral tilting vividly appears. The ABF images along the [1$\bar{1}$0] projection also show no evident differences in the octahedral tilting between Bi- and Na-excess tetragonal phases. Even though there is no apparent difference in the atomic array between Na- and Bi-excess areas, there should be a clear disparity between them based on a consideration of the local charge balance induced by compositional disordering. Bi- and Na-excess areas create positive and negative charges,

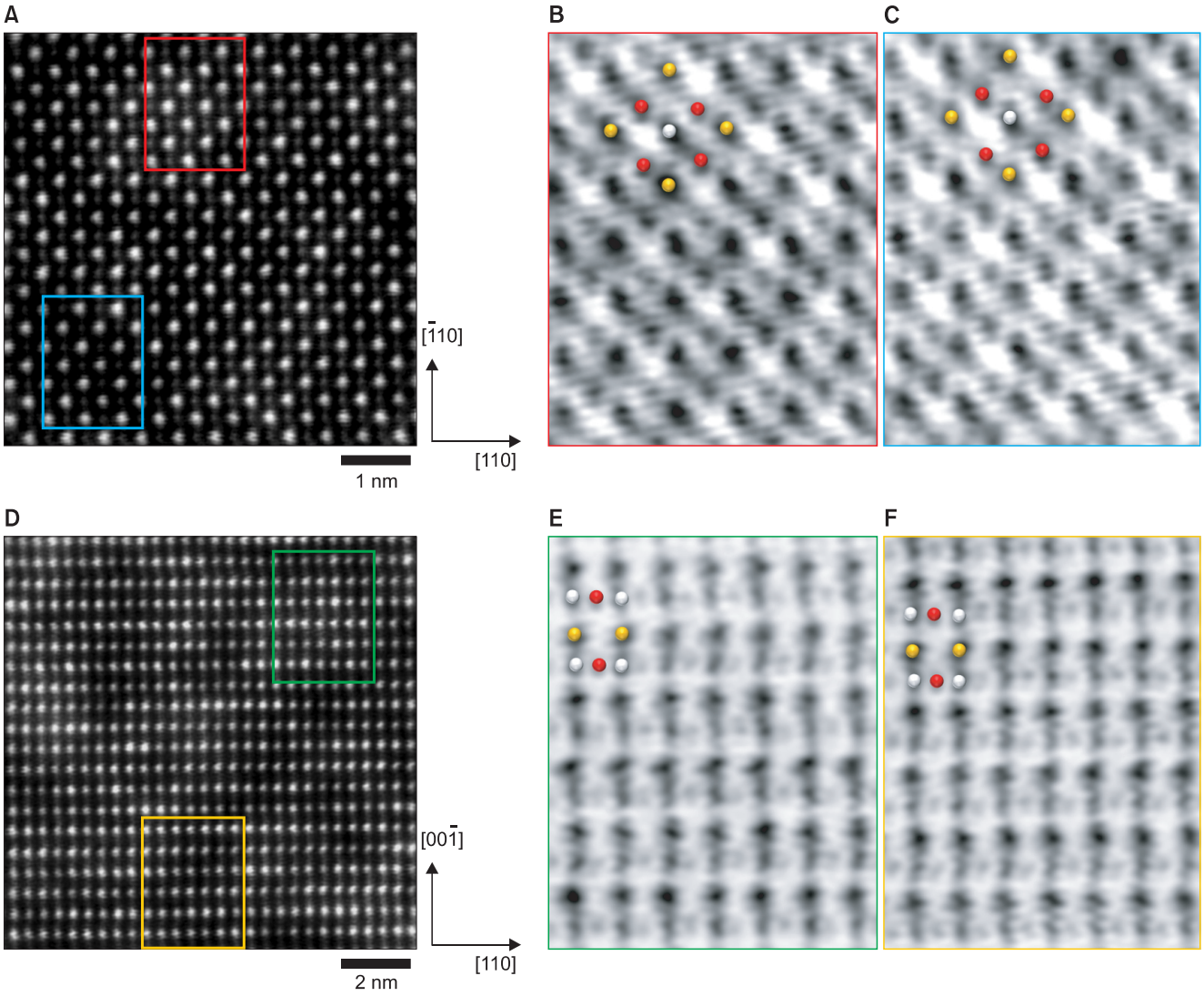

Fig. 4. (A) and (D) are HAADF-STEM images from NBT along [001] and [1$\bar{1}$0] projections, respectively. (B) and (C) are magnified ABF-STEM images from the region indicated by the red and blue rectangles in image (A), respectively. (E) and (F) are magnified ABF-STEM images from the region indicated by green and orange rectangles in image (D). The unit cell structure along the [001] or [1$\bar{1}$0] projections was superimposed into each ABF image, where the orange, gray, and red spheres indicate A-site (Na & Bi), Ti, and O atomic columns, respectively. HAADF, high-angle annular dark-field; STEM, scanning transmission electron microscopy; NBT, $Na_{1/2}Bi_{1/2}TiO_3$; ABF, annular bright field.

because the average charge of the A-site is supposed to be +2. Therefore, there is expected to be a lower-dimensional defects cluster in each region, which does not critically affect the atomic displacement.

To this end, we performed EELS measurements in STEM mode using ~1 Å probe size and obtained *O-K* edge and

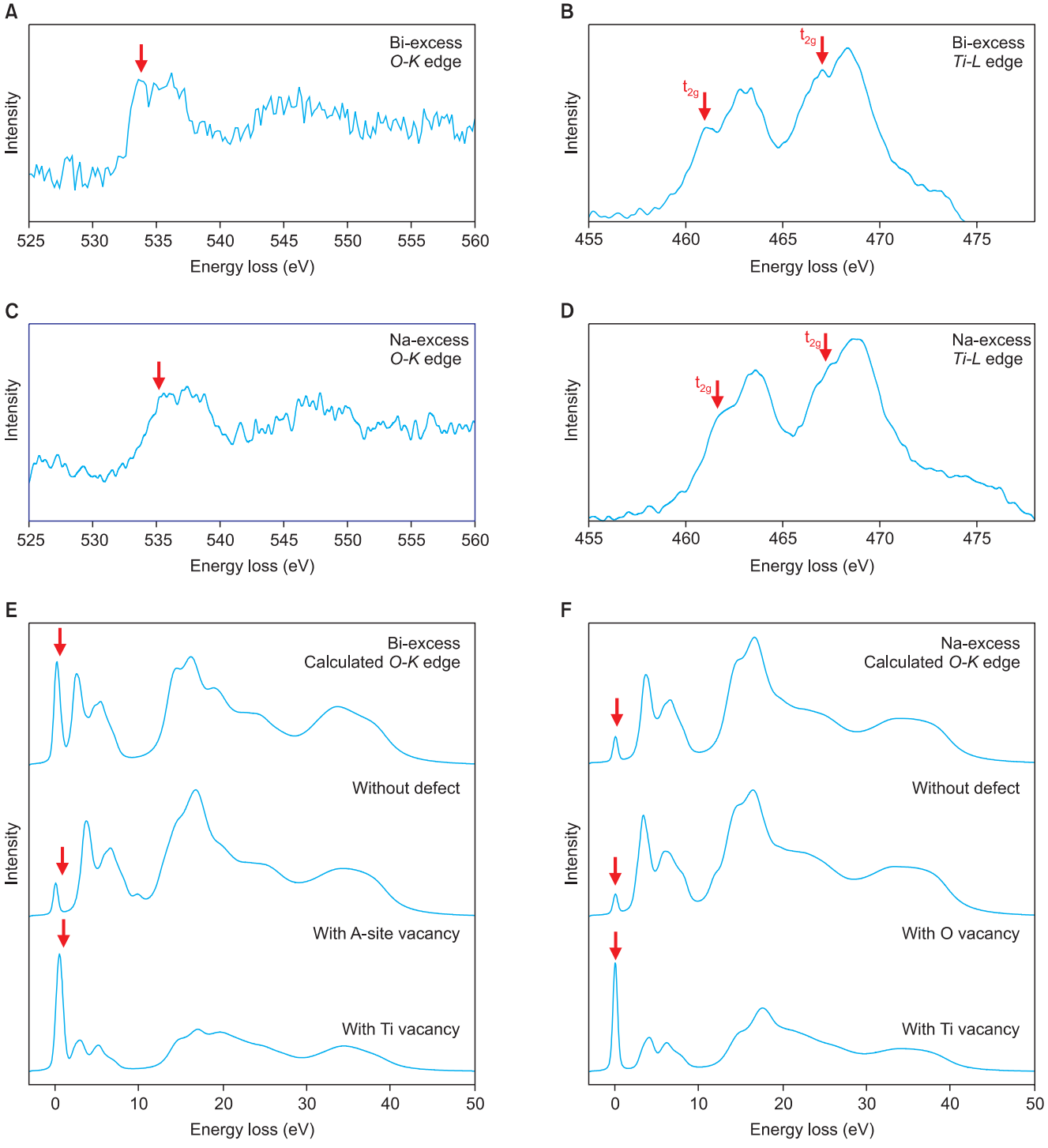

Fig. 5. (A) and (B) are the experimentally obtained *O-K* and *Ti-L* edges from a Bi-excess area. (C) and (D) are the experimentally obtained *O-K* and *Ti-L* edges from a Na-excess area. (E) shows the calculated *O-K* edge structures from Bi-excess models: pure Bi-excess, Bi-excess with a A-site vacancy, and Bi-excess with a titanium vacancy. (F) shows the calculated *O-K* edge structures from Na-excess models: Na-excess NBT, Na-excess NBT with an oxygen vacancy, and Na-excess NBT with a titanium vacancy. NBT, $Na_{1/2}Bi_{1/2}TiO_3$.

Ti-L edge structures from Na- and Bi-excess areas, since the EELS structure is sensitive to the formation of point defects. Fig. 5A and 5C are *O-K* edges recorded from Bi- and Na-excess areas, respectively. The first peak at ~534 eV indicated by the red arrow is the peak that should be noted, since the EELS calculation results revealed that this peak is mainly affected by compositional disordering and defect formation, as shown in Fig. 5E and F. To predict the *O-K* edge structure of EELS, a 2×2×3 supercell structure was constructed and Bi (Na)-excess structure was assumed to have A-sites of 70% Bi (Na) and 30% Na (Bi). The simulated *O-K* edge from the Bi-excess structure without introducing any atomic defects is shown in Fig. 5E, which is found to be inconsistent with the experimental *O-K* edge from the Bi-excess area. This indicates a significant occurrence of atomic defects. As aforementioned, the Bi-excess structure is capable of creating positive charges and subsequently negatively charged cationic vacancies are expected to generate to build up a local charge balance. Therefore, a Bi-excess structure for calculation was constructed with an A-site vacancy and then an *O-K* edge structure was calculated as shown in Fig. 5E. Interestingly, the first peak is largely decreased by an A-site vacancy and thus the calculated *O-K* edge become consistent with the experimental *O-K* edge of Fig. 5A. This means that the Bi-excess areas by compositional disordering create and accumulate A-site vacancies.

As for the Na-excess area, the *O-K* edge of Fig. 5C is quite similar to that from the Bi-excess area (Fig. 5A), where the first peak is also significantly diminished. The Na-excess area is negatively charged and thus is expected to be compensated by the positively charged oxygen vacancies. However, the calculated *O-K* edges from the Na-excess structure exhibit no distinguishable differences regardless of incorporation of oxygen vacancies, as shown in Fig. 5F, and both calculated *O-K* edges are similar to the experimental *O-K* edge from the Na-excess area; therefore, the *O-K* edge is no longer useful to characterize the formation of an oxygen vacancy in the Na-excess area. Fortunately, however, the *Ti-L* edge is known to be

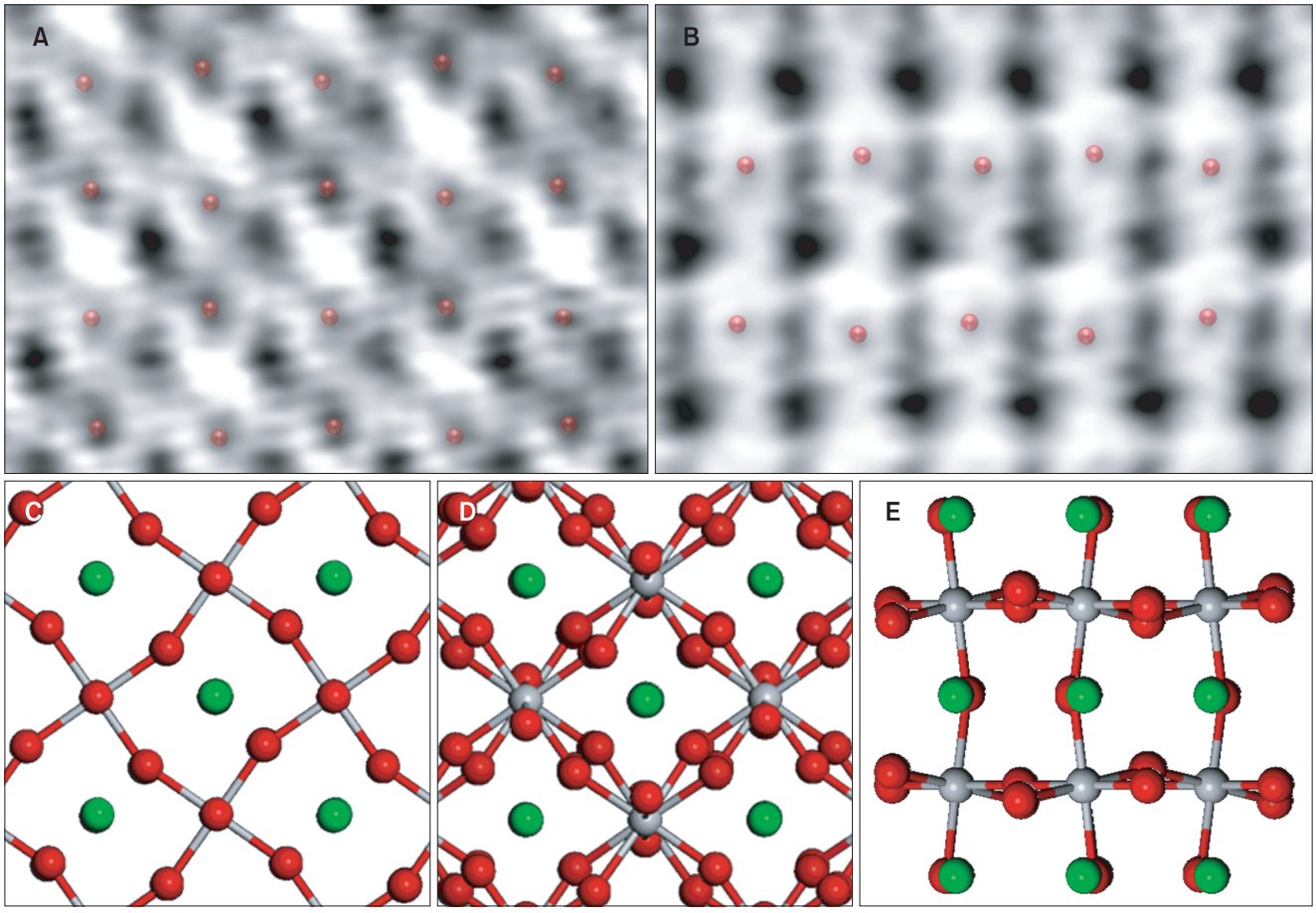

Fig. 6. The enlarged ABF-STEM images from (A) [001] and [1$\bar{1}$0] projections. The inserted red spheres in (A) and (B) indicate the location of oxygen columns. The schematic structures of (C) $a^0a^0c^+$ and (D) $a^-a^-a^-$ octahedral tilting appear with respect to [001] projection. (D) The schematic structure of $a^-a^0a^0$ octahedral tilting is shown via [110] projection. The green, gray, and red spheres indicate A-site (Na & Bi), Ti, and O atomic columns, respectively. ABF, annular bright field; STEM, scanning transmission electron microscopy.

very applicable to determine the existence of oxygen vacancies in perovskite ceramics (Klie & Browning, 2000; Muller et al., 2004; Mizoguchi et al., 2010), since the disappearance of its t_{2g} can be clearly observed by the formation of oxygen vacancies, which is related with the transition of the Ti-valence state from +4 to +3. The appearance of t_{2g} in the *Ti-L* spectrum is due to the strong covalence state between the d-shell of Ti and the p-shell of O; thus the decrease in the intensity of t_{2g} directly indicates a weaker covalence state between titanium and oxygen, thereby implying a decrease in the valence state of titanium. Therefore, the experimental *Ti-L* edge of Fig. 5D clearly demonstrates that the Na-excess area is compensated by the oxygen vacancies. The calculated *O-K* edges in the case of incorporation of a titanium vacancy (Fig. 5E and F) show that the first peaks appear to become stronger in both Bi- and Na-excess structures, and therefore a titanium vacancy formation should be outside of consideration. Therefore, the determined O/Ti ratios deduced by *O-K* and *Ti-L* edges obtained from Bi- and Na-excess areas provide quantitative information on the amount of oxygen vacancies. Under the assumption that there is neither a titanium vacancy nor an oxygen vacancy in the Bi-excess area, the measured O/Ti ratio, 1.85, can be stoichiometrically normalized to 2. The normalized O/Ti ratio from the Na-excess area is thus found to be 1.53 and therefore ~23.5% of oxygen atoms are expected to evacuate to compensate the charge imbalance induced by the compositional disordering.

Finally, it deserves mentioning the ambiguity in the octahedral tilting. First, despite the chemical inhomogeneity and local atomic defects, the long-range octahedral tilting is maintained as shown in Figs. 4 and 6. Second, the octahedral tilting structure is not consistent with proposed models. Fig. 6C and D show the $a^0a^0c^+$ octahedral tilting in nonpolar tetragonal structure and $a^-a^-a^-$ octahedral tilting in polar rhombohedral structure, respectively. Since the atomic structure is thought to be related with the nonpolar tetragonal phase, the octahedral tilting of Fig. 6A is supposedly comparable to $a^0a^0c^+$ tilting. However, the recorded ABF image of Fig. 6A seems to be consistent with neither $a^0a^0c^+$ (Fig. 6C) nor $a^-a^-a^-$ octahedral tilting (Fig. 6D). In the case of [1$\bar{1}$0] projection (Fig. 6B), the oxygen position is aligned in a zig-zag way but this alignment cannot be explained by $a^0a^0c^+$ or $a^-a^-a^-$ octahedral tilting, either. Instead, this zig-zag alignment is deduced from $a^-a^0a^0$ or $a^-a^-a^0$ octahedral tilting, as shown in Fig. 6E. Observed octahedral tilting in our ABF STEM experiments is not feasibly understood by the previously proposed models. The ambiguous octahedral tilting in this study might be related with the third party candidate for octahedral tilting and therefore the careful analysis using neutron diffraction or Raman spectroscopy should be carried out in parallel. The other plausible possibility is that the positively charged oxygen vacancies and negatively charged A-site cationic vacancies are distributed in an ordered way to compensate the charge imbalance and it gives rise to the unexpected octahedral tilting, because the analyzed NBT is the as-sintered sample without any poling process. To avoid the problematic issue, it is necessary to analyze the atomic structure of the electrically poled NBT sample, which stabilizes the atomic displacement as well as the octahedral tilting via the redistribution of the charged vacancies.

CONCLUSIONS

By using the aberration-corrected STEM technique, we could visually confirm that NBT has no superlattice structure but compositional disordering inhomogeneously occurs. Na- and Bi-excess areas are inhomogeneously distributed through all samples but this A-site cationic disordering does not significantly affect either the atomic structure or the octahedral tilting. However, the charge imbalance caused by the cationic disordering is compensated by the vacancy formation: Na- and Bi-excess areas hold oxygen vacancies and A-site vacancies, respectively. Even though coexistence of the polar and nonpolar phases is examined via electron diffraction analysis, the PNRs could not be observed via atomic scale STEM analysis. Though ABF STEM analysis, the octahedral tilting is directly visualized but none of the proposed models in terms of octahedral tilting in NBT is comparable to the experimentally observed octahedral tilting.

REFERENCES

Bao P, Yan F, Li W, Dai Y R, Shen H M, Zhu J S, Wang Y N, Chan H L W, and Choy C-L (2002) Mechanical properties related to the relaxor-ferroelectric phase transition of titanium-doped lead magnesium niobate. *Appl. Phys. Lett.* **81**, 2059-2061.

Batson P E, Dellby N and Krivanek O L (2002) Sub-angstrom resolution using aberration corrected electron optics. *Nature* **418**, 617-620.

Bokov A A, Leshchenko M A, Malitskaya M A and Raevski I P (1999) Dielectric spectra and Vogel-Fulcher scaling in Pb(In0.5Nb0.5)03 relaxor ferroelectric. *J. Phys.: Condensed Matter* **11**, 4899-4911.

Burton B P and Cockayne E (2001) Prediction of the Na1/2Bi1/2TiO3 ground state. *AIP Conference Proceedings in Fundamental Physics of Ferroelectrics* **582**, 82-90.

Chiang Y-M, Farrey G W and Soukhojak A N (1998) Lead-free high-strain single-crystal piezoelectrics in the alkaline–bismuth–titanate perovskite family. *Appl. Phys. Lett.* **73**, 3683-3685.

Choi S-Y, Chung S-Y, Yamamoto T, and Ikuhara Y (2009) Direct determination of dopant site selectivity in ordered perovskite CaCu3Ti4012 polycrystals by aberration-corrected STEM. *Adv. Mater.* **21**, 885-889.

Choi S-Y, Jeong S-J, Lee D-S, Kim M-S, Lee J-S, Cho J H, Kim B I, and Ikuhara Y (2012) Gigantic electrostrain in duplex structured alkaline niobates. *Chem. Mater.* **24**, 3363-3369.

Chu F, Setter N and Tagantsev A K (1993) The spontaneous relaxor-ferroelectric transition of Pb(Sc0.5Ta0.5)03. *J. Appl. Phys.* **74**, 5219-5134.

Chung S-Y, Choi S-Y, Yamamoto T and Ikuhara Y (2008) Atomic-scale visualization of antisite defects in LiFeP04. *Phys. Rev. Lett.* **100**, 125502-1-125502-4.

Chung S-Y, Choi S-Y, Yamamoto T and Ikuhara Y (2009) Orientation-Dependent Arrangement of Antisite Defects in Lithium Iron(II) Phosphate Crystals. *Angew. Chem. Int. Ed.* **48**, 543-546.

Dai X, Xu Z and Viehland D (1994) The spontaneous relaxor to normal ferroelectric transformation in La-modified lead zirconate titanate. *Phil. Mag. B* **71**, 33-38.

Dorcet V, Trolliard G and Boullay P (2008a) Reinvestigation of phase transitions in Na0.5Bi0.5TiO3 by TEM. Part I: First order rhomboheral to orthorhombic phase transition. *Chem. Mater.* **20**, 5061-5073.

Dorcet V, Trolliard G and Boullay P (2008b) Reinvestigation of phase transitions in Na0.5Bi0.5TiO3 by TEM. Part II: Second order orhorhombic to tetragonal phase transition. *Chem. Mater.* **20**, 5074-5082.

Dorcet V and Troillard G (2008) A transmission electron microscopy study of the A-site disordered perovskite Na0.5Bi0.5TiO3. *Acta. Mater.* **56**, 1753-1761.

Findlay S D, Shibata N, Sawada H, Okunishi E, Kondo Y, and Ikuhara Y (2010) Dynamics of annular bright field imaging in scanning transmission electron microscopy. *Ultramicroscopy* **110**, 903-923.

Haider M, Uhlemann S, Schwan E, Kabius B, Rose H, and Urban K (1998) Electron microscopy image enhanced. *Nature* **392**, 768-769.

Hovden R, Xin H L, and Muller D A (2010) Extended depth of field for high-resolution scanning transmission electron microscopy. *Microsc. Microanal.* **17**, 75-80.

Ishikawa R, Okunishi E, Sawada H, Kondo Y, Hosokawa F, and Abe E (2010) Direct imaging of hydrogen-atom columns in a crystal by annular bright-field electron microscopy. *Nature Mater.* **10**, 278-281.

Jia C L, Mi S-B, Urban K, Vrejoiu I, Alexe M, and Hesse D (2008) Atomic-scale study of electric dipoles near charged an uncharged domain walls in ferroelectric films. *Nature Mater.* **7**, 57-61.

Jones G O and Thomas P A (2000) The tetragonal phase of Na0.5Bi0.5TiO3 – a new variant of the perovskite structure. *Acta. Cryst. B* **56**, 426-430.

Jones G O and Thomas P A (2002) Investigation of the structure and phase transitions in the novel A-site substituted distorted perovskite compound Na0.5Bi0.5TiO3. *Acta. Cryst. B* **58**, 168-178.

Klie R F and Browning N D (2000) Atomic scale characterization of oxygen vacancy segregation at SrTiO3 grain boundaries. *Appl. Phys. Lett.* **87**, 3737-3739.

Kreisel J, Glazer A M, Bouvier P, and Lucazeau G (2001) High-pressure Raman study of a relaxor ferroelectric: the Na1/2Bi1/2TiO3 perovskite. *Phys. Rev. B* **63**, 174106-1-174106-10.

Kreisel J, Glazer A M, Jones G, Thomas P A, Abello L, and Lucazeau G (2000) An x-ray diffraction and Raman spectroscopy investigation of A-site substituted perovskite compounds: the (Na1-xKx)0.5Bi0.5TiO3 ($0 < x < 1$) solid solution. *J. Phys.: Condensed Matter* **12**, 3627-3280.

Krunmins A, Shiosaki T, and Koizumi S (1994) Spontaneous trasition between relaxor and ferroelectric states in lanthanum-modified lead zirconate titanate (6–7)/65/35. *Jpn. J. Appl. Phys.* **33**, 4940-4945.

Levin I and Reaney I M (2012) Nano-and mesoscale structure of Na1/2Bi1/2TiO3: a TEM perspective. *Adv. Func. Mater.* **22**, 3445-3452.

Lupini A R and Pennycook S J (2007) Aberration corrected imaging in the STEM. *Microsc. Microanal.* **13**, 1146-1147.

Mizoguchi T, Olovsson W, Ikeno H and Tanaka I (2010) Theoretical ELNES using one-particle and multi-particle calculations. *Micron* **41**, 695-709.

Muller D A, Nakagawa N, Ohtomo A, Grazul J L, and Hwang H Y (2004) Atomic-scale imaging of nanoengineered oxygen vacancy profiles in SrTiO3. *Nature* **430**, 657-661.

Nellist P D, Chisholm M F, Dellby N, Krivanek O L, Murfitt M F, Szilagy Z S, Lupini A R, Borisevich A, Sides Jr. W H, and Pennycook S J (2004) Direct sub-angstrom imaging of a crystal lattice. *Science* **305**, 1741.

Okunishi E, Ishikawa I, Sawada H, Hosokawa F, Hori M, and Kondo Y (2009) Visualization of light elements at ultrahigh resolution by STEM annular bright field microscopy. *Microsc. Microanal.* **15**, 164-165.

Park S-E, Chung S-J, Kim I-T, and Hong K S (1994) Nonstoichiometry and the long-range cation ordering in crystals of (Na1/2Bi1/2) TiO3. *J. Am. Ceram. Soc.* **77**, 2641-2647.

Petzelt J, Kamba S, Fabry J, Noujni D, Porokhonskyy V, Pashkin A, Franke I, Roleder K, Suchanicz J, Klein R, and Kugel G E (2004) Infrared, Raman and high-frequency dielectric sspectroscopy and the phase transition in Na1/2Bi1/2TiO3. *J. Phys.: Condensed Matter* **16**, 2719-2731.

Sciau P, Calvarin G, and Ravez J (2000) X-ray diffraction study of BaTi0.65Zr0.3503 and Ba0.92Ca0.08Ti0.75Zr0.2503 compositions: influence of electric field. *Sol. Stat. Commun.* **113**, 77-82.

Simon A, Ravez J J, and Maglione M (2004) The crossover from a

ferroelectric to a relaxor state in lead-free solid solutions. *J. Phys.: Condensed Matter* **16**, 963.

Siny G, Smirnova T A, and Krunzina T V (1991) The phase transition dynamics in Na1/2Bi1/2TiO3. *Ferroelectrics* **124**, 207-212.

Smolenskii G A, Isupov V A, Agranovskaya A I, and Krainik N N (1961a) New ferroelectrics of complex composition. *Sov. Phys. Solid State* **2**, 2651-2654.

Smolenskii G A, Isupov V A, Agranovskaya A I, and Popov S N (1961b) Ferroelectrics with diffuse phase transitions. *Sov. Phys. Solid State* **2**, 2584-2594.

Tagantsev A K and Galzounov A E (1998) Mechanism of polarization response in the ergodic phase of a relaxor ferroelectric. *Phys. Rev. B* **57**, 18-21.

Tai C W and Lereah Y (2009) Nanoscale oxygen octahedral tilting in 0.90(Bi1/2Na1/2)TiO3–0.05(Bi1/2K1/2)TiO3–0.05BaTiO3 lead-free perovskite piezoelectric ceramics. *Appl. Phys. Lett.* **95**, 062901-1-062901-3.

Tu C S, Siny I G, and Schmidt V H (1994) Brillouin scattering in Na1/2Bi1/2TiO3. *Ferroelectrics* **152**, 403-408.

Vakhrushev S B, Isupov V A, Kvyatkovsky B E, Okuneva N M, Pronin I P, Smolensky G A, and Syrnikov P P. Phase transition and soft modes in sodium bismuth titanate. *Ferroelectrics* **63**, 153-160.

Xu Y-N and Ching W Y (2000) Electronic structure of Na1/2Bi1/2TiO3 and its solid solution with BaTiO3. *Phy. Mag. B* **80**, 1141-1151.

Yao J, Ge W, Yan Li, Reynolds W T, Li J, Viehland D, Keselev D A, Kholkin A L, Zhang Q, and Luo H (2012) The influence of Mn substitution on the local structure of Na0.5Bi0.5TiO3 crystals: increased ferroelectric ordering and coexisting octahedral tilts. *J. Appl. Phys.* **111**, 064109-1-064109-6.

Yasuda N, Ohwa H, and Asano S (1996) Dielectric properties and phase transitions of Ba(Ti1-xSnx)03 solid solution. *Jpn. J. Appl. Phys.* **35**, 5099.